Power Electronic Systems
Laboratory

© 2018 IEEE

Proceedings of the IEEE Energy Conversion Congress and Exposition (ECCE USA 2018), Portland, OR, USA, September 23-27, 2018

**High-Efficiency Weight-Optimized Fault-Tolerant Modular Multi-Cell Three-Phase GaN Inverter for Next Generation Aerospace Applications**

M. Guacci,
D. Bortis,
J. W. Kolar

Personal use of this material is permitted. Permission from IEEE must be obtained for all other uses, in any current or future media, including reprinting/republishing this material for advertising or promotional purposes, creating new collective works, for resale or redistribution to servers or lists, or reuse of any copyrighted component of this work in other works.

Eidgenössische Technische Hochschule Zürich
Swiss Federal Institute of Technology Zurich

# High-Efficiency Weight-Optimized Fault-Tolerant Modular Multi-Cell Three-Phase GaN Inverter for Next Generation Aerospace Applications

Mattia Guacci, *Student Member, IEEE,* Dominik Bortis, *Member, IEEE,* and Johann W. Kolar, *Fellow, IEEE*
Power Electronic Systems Laboratory, ETH Zurich, Switzerland

Corresponding Author: Mattia Guacci, ETL I12, Physikstrasse 3, 8092 Zurich, Switzerland
e-mail: guacci@lem.ee.ethz.ch

***Abstract*— The aircraft industry demands a significant increase in terms of efficiency and gravimetric power density of power converters for next generation aerospace applications. Between the two minimum targets, i.e. an efficiency $> 98\,\%$ and a gravimetric power density $> 10\,\mathrm{kW/kg}$, the specification concerning the converter weight is the most challenging to fulfill. Since cooling systems and magnetic components dominate the weight breakdown of conventional converter concepts, multi-cell topologies, enabling improved semiconductors performance and reduced filtering requirements, are foreseen as promising solutions for the power electronics on board of *More Electric Aircraft*. On the other hand, the necessary simultaneous operation of a high number of cells inevitably limits the reliability of multi-cell converters if redundancy is not provided. In this paper, a favorable scaling trend of power density with respect to reliability, aiming to guarantee fault-tolerant operation without affecting the performance figures, is identified in modular multi-cell converters. Thus, a $45\,\mathrm{kW}$ weight-optimized modular multi-cell three-phase inverter featuring a redundant power stage is optimized, achieving an efficiency of $99\,\%$ and a gravimetric power density of $22.8\,\mathrm{kW/kg}$.**

***Index Terms*— Modular Multi-Cell Inverter, Figure of Merit of Power Semiconductors, Power Converters Reliability, Multi-Objective Optimization, More Electric Aircraft.**

## I. Introduction

Driven by the advantages enabled by *More Electric Aircraft* (MEA) concepts, i.e. decreased fuel consumption and $CO_2$ and $NO_x$ emissions reduction, in 2010 the electric power demand of commercial airplanes surpassed the $1\,\mathrm{MVA}$ milestone on-board of *Boeing 787* [1]. As a consequence of the established next steps towards *More Electric Engine* (MEE), this figure is expected to double in 2020, i.e. when the maiden flight of a $2\,\mathrm{MW}$ hybrid-electric propulsion system, developed in a collaboration among *Airbus*, *Siemens* and *Rolls-Royce* [2], is scheduled. Furthermore, according to *Airbus*'s forecasts, the power requirements of next generation single aisle aircraft should finally reach $20\,\mathrm{MW}$ in the next decades [3].

Motivated by these trends, the power electronics roadmap for next generation aerospace applications is targeting to significantly improve efficiency ($\eta$) and gravimetric power density ($\gamma$) of power converters [4]. As an example, **Fig. 1** compares the goals in the $\eta\gamma$-performance space of two on-going projects focusing on MEA with the figures of comparable (in terms of power rating) state-of-the-art prototypes (yellow dots). The *Horizon2020* European Project 636170 - *Integrated, Intelligent Modular Power Electronic Converter* (I2MPECT) [5] (red dots) and the NASA Government Contract NNX14AL79A - *High Speed, High Frequency Air-Core Machine and Drive* [6], [7] (blue dots) set the minimum targets at $\eta = 98\,\%$ and $\gamma = 10\,\mathrm{kW/kg}$. From the comparison in **Fig. 1**, it becomes evident that the most demanding improvement concerns $\gamma$. The reason is identified in the fact that for each kg on board of an aircraft roughly $1.7\,\mathrm{t}$ of fuel are burned and $5.4\,\mathrm{t}$ of $CO_2$ are emitted per year from all the air traffic [1]. Thus, a reduction of weight can significantly help to meet the lowered emissions target [1].

The weight breakdown analysis of modern power converters reveals that magnetic and filter components and cooling systems are the principal contributors to the overall converters weight [8]. Increasing the switching frequency in conventional inverter topologies (to reduce magnetic components volume and weight) faces a trade-off with maintaining a high-efficiency, therefore different approaches must be evaluated. Moreover, the growing power demand on board of MEA is inevitably accompanied by an increasing DC-link voltage of the installed energy distribution network, e.g. from the actual $540\,\mathrm{V}$ [5] to the $3\,\mathrm{kV}$ of the mentioned MEE prototype [3] (and reasonably further). Thus, as occurred in medium-voltage (MV) applications, conventional converter solutions will face limitations, e.g. in terms of power devices blocking voltage and capacitors availability [9]. Finally, high reliability, scalability, and reduced design and maintenance efforts are key features in the aircraft industry [10], hence also these aspects must be considered in the selection of alternative topologies. Multi-cell converters enable improved semiconductor performance and the downsizing of the magnetic components because of the diminished harmonic content of their voltage waveforms [11]. Consequently, they are identified as a candidate approach to meet the defined performance targets. Unfortunately, their increased complexity inevitably worsen the system reliability, thus providing redundancy becomes mandatory. The effectiveness of this strategy is proven with a decade of successful operation in MV applications [12].

Only modular multi-cell topologies can combine high reliability with superior $\eta\gamma$-performance, since few redundant cells, which have a negligible impact on the converter power density, are sufficient to achieve even higher reliability figures than conventional solutions [13]. Their modular structure additionally ensures straight-forward scalability, facilitating a flexible design procedure [9].

Ultimately, in order to extend the advantages of modularity also to the electric machines connected to these converters, e.g. compressor units for the environmental control system, multi-phase inverters (and accordingly machines) are preferred [14]. In this case, fault-tolerant operation after a partial (involving one or few phases) failure is ensured, increasing the overall system reliability. Moreover, when the power electronics is integrated in the machine housing, additional advantages, e.g. in terms of system power density and installation costs and complexity, are enabled [15].

The goal of this paper is to investigate the achievable $\eta\gamma$-performance of a fault-tolerant modular multi-cell three-phase inverter designed

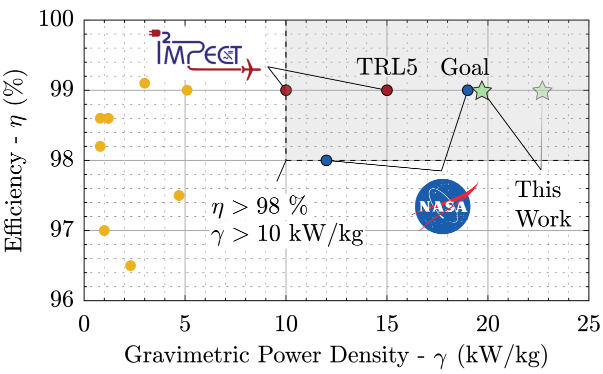


**Fig. 1:** $\eta\gamma$-performance space presenting the performance goal ($\eta > 98\,\%$ and $\gamma > 10\,\mathrm{kW/kg}$) of on-going projects focusing on power electronics for next generation aerospace applications and the result of this work. The $\gamma$-target is significantly higher compared to the figures of state-of-the-art prototypes.

This work was supported by the Swiss State Secretariat for Education, Research and Innovation (SERI) under contract number 15.0161. The opinions expressed and arguments employed herein do not necessarily reflect the official views of the Swiss Government.

**TABLE I:** Specifications of the considered three-phase inverter.

| Parameter | Description | Nominal Value |
|---|---|---|
| $V_{dc}$ | DC-link voltage | 1000 V |
| $P_{out}$ | output power | 45 kW |
| $f_{out}$ | output frequency | 2 kHz |
| $M_{index}$ | modulation index | 0.9 |

according to the requirements of next generation aerospace applications and to the specifications given in **Table I**. Section II discusses an analytical study, based on loss models and figures of merit, comparing the semiconductors performance in conventional and multi-cell inverter topologies. Section III introduces the reliability figures of multi-cell converters and evaluates the impact of different redundancy approaches on their power density. Section IV presents the trend towards Integrated Modular Motor Drives (IMMD) applied to modular multi-cell inverters. Since the Stacked Polyphase Bridge (SPB) converter combines all the highlighted features, it is finally identified as the best candidate solution to fulfill the targeted performance. Hence, it is optimized in Section V for the specifications of interest, achieving $\eta = 99\,\%$ and $\gamma = 22.8\,{}^{\mathrm{kW}}/_{\mathrm{kg}}$ ($19.2\,{}^{\mathrm{kW}}/_{\mathrm{kg}}$ adding one redundant cell, cf. **Fig. 1**). Section VI summarizes the results of this work.

## II. Performance Analysis of Power Semiconductors

The switching and conduction losses in the semiconductors dominate the loss breakdown of modern power converters featuring a high power density [16]. Hence, accurate loss models based on the characteristics of state-of-the-art semiconductors can provide sensible estimations of their overall performance and enable the comparison in terms of efficiency among different converter concepts. Therefore, with the final aim of designing a 99 %-efficient 45 kW weight-optimized three-phase inverter, a semiconductors performance study is presented in this section.

### *A. Loss Models of Power Semiconductors*

The semiconductors loss analysis is based on a conventional phase-leg, for which switching and conduction loss models are developed and discussed herein.

In case of an hard-switching transition, the switching losses $P_{sw}$ are separated in current independent and current dependent fractions [17]. The switching losses of soft-switching transitions are neglected, since proven to be typically one order of magnitude smaller [18]. The current independent fraction of $P_{sw}$, i.e. $P_{sw,oss} = f_{sw} V_{dc} Q_{oss}\big|_{V_{dc}}$ models the losses due to the charging and discharging processes of the parasitic output capacitance $C_{oss}$ of the power semiconductors, with $Q_{oss}\big|_{V_{dc}}$ indicating the charge stored in $C_{oss}$ when charged from 0 V to the DC voltage $V_{dc}$. If present, the additional charge $Q_{rr}$ associated to the reverse recovery phenomenon should be added to $Q_{oss}$, but is neglected herein.

The current dependent fraction of $P_{sw}$, i.e. $P_{sw,vi} = f_{sw} {}^{1}/_{2} V_{dc} I_{sw} \left(t_{r,i} + t_{f,v}\right)$ is caused by the simultaneous existence of $V_{dc}$ and of the switched current $I_{sw}$ at the terminals of the turning on device. An experimental validation of this model can be observed analyzing a hard-switching transition of a phase-leg, e.g. in a double-pulse test setup with inductive load: first the device current $i_{ds}$ linearly rises with a fixed ${}^{\mathrm{d}i_{ds}}/_{\mathrm{d}t}$ until $I_{sw}$ is reached, while the voltage across the device $v_{ds}$ is clamped to $V_{dc}$. As soon as $i_{ds} = I_{sw}$ (if the reverse recovery phenomenon is neglected), $v_{ds}$ starts to quasi-linearly decrease from $V_{dc}$ to 0 V with a fixed ${}^{\mathrm{d}v_{ds}}/_{\mathrm{d}t}$. Expressing the current rise time $t_{r,i}$ and the voltage fall time $t_{f,v}$ as ${}^{I_{sw}}/_{\mathrm{d}i_{ds}/\mathrm{d}t}$ and ${}^{V_{dc}}/_{\mathrm{d}v_{ds}/\mathrm{d}t}$ respectively, highlights the possible reduction of switching losses, or the complementary increase of switching frequency $f_{sw}$, enabled by fast switching power semiconductors (e.g. Silicon-Carbide (SiC) and Gallium-Nitride (GaN)). Additionally, it clarifies how this benefit vanishes if the maximum switching speed is limited from external factors: for example, partial discharge induced motor windings isolation aging and over-voltage due to wave reflections in case of long motor cables are typical reasons to limit the ${}^{\mathrm{d}v_{ds}}/_{\mathrm{d}t}$ below $10\,{}^{\mathrm{V}}/_{\mathrm{ns}}$ [19], whereas voltage oscillation and overshoot at the gate terminal or at the switch node define the maximum ${}^{\mathrm{d}i_{ds}}/_{\mathrm{d}t}$ [20].

**TABLE II:** Fitting coefficients of the FoM model $aV^k$.

| | Si | GaN | SiC |
|---|---|---|---|
| $a$ | $1.23 \cdot 10^{13}$ | $1.63 \cdot 10^{12}$ | $2.55 \cdot 10^{12}$ |
| $k$ | $-2.05$ | $-1.40$ | $-1.48$ |
| $V_{ds,MAX}$ (V) | 75 ... 900 | 100 ... 650 | 650 ... 1700 |

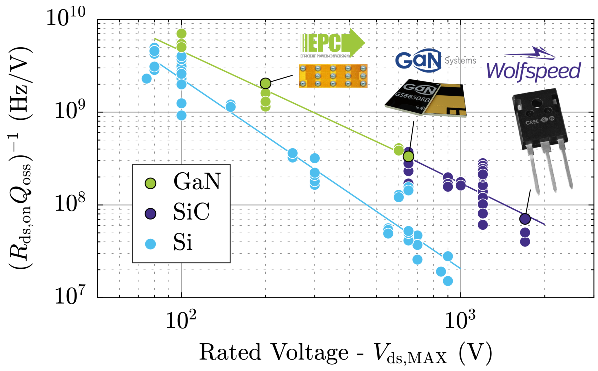


**Fig. 2:** FoM calculated as ${}^{1}/_{(R_{ds,on} Q_{oss})}$ of most of the commercially available Si, SiC and GaN power semiconductors as function of their blocking voltage. The model FoM $= aV^k$ with the fitting coefficients reported in **Table II** best interpolates the data.

The conduction losses $P_{cond}$ are calculated as $R_{ds,on} I^2_{out,RMS}$, where $R_{ds,on}$ is the on-state resistance of the power semiconductors alternatingly conducting the phase current. Sinusoidal phase current and voltage with peak values $V_{out} = {}^{V_{dc}}/_{2}$ (no third harmonic injection) and $I_{out} = {}^{2P_{out}}/_{V_{out}}$, i.e. $I_{out,RMS} = {}^{2\sqrt{2}P_{out}}/_{V_{dc}}$, are assumed. Finally, $P_{semi} = P_{sw} + P_{cond}$ constitutes the overall semiconductors losses.

### *B. Figure of Merit of Power Semiconductors*

The accuracy of the proposed loss models heavily depends on the underpinning parameters, e.g. $R_{ds,on}$ and $Q_{oss}$. A practical approach to consider and compare different power semiconductors is based on the corresponding figures of merit (FoM) and is introduced in this section [21]. A FoM consists of a numeric value obtained combining several characteristics of a device (e.g. a power semiconductor), appropriately selected to be representative of its performance. The FoM calculated as ${}^{1}/_{(R_{ds,on} Q_{oss})}$ [22] is considered as a promising indicator for the analysis of interest and therefore preferred [23]. **Fig. 2** summarizes the selected FoM of more than hundred commercially available Silicon (Si), SiC and GaN power semiconductors as function of their blocking voltage $V_{ds,MAX}$ (75 V ... 1.7 kV). As can be noticed, a linear trend characterizes each semiconductor material in logarithmic-scale, hence

$$\mathrm{FoM}(V) = \frac{1}{R_{ds,on} Q_{oss}\big|_{V}} = aV^k \tag{1}$$

best interpolates the data. The coefficients of the model, different for each semiconductor, are reported in **Table II**. It is worth noticing how

- GaN and SiC (comparable with each other) outperform Si as a result of their higher breakdown electric field and bandgap energy, and that
- all FoM trends scale over-proportionally with respect to voltage since $|k| > 1$ in all cases.

### *C. Conventional Inverter Concept*

The proposed semiconductors loss models and FoM are combined in this section to evaluate the $\eta$-limit of a conventional inverter phase-leg. The specifications of **Table I** are considered as reference for one phase-leg, i.e. $V_{dc} = 1000$ V and $P_{out,phase} = 15$ kW. The values of $R_{ds,on}$ and $Q_{oss}$ are calculated (eventually extrapolated) with the fitting coefficients of the FoM model (**Table II**). In this ideal approximation $V = V_{dc} = V_{ds,MAX}$ is assumed, whereas in a real design a certain margin between $V_{dc}$ and $V_{ds,MAX}$ is necessary, e.g. $V_{dc} \leq {}^{2}/_{3} V_{ds,MAX}$.

To eliminate in a first step the dependency from the mentioned switching speed constraints, ${}^{di_{ds}}/_{dt}$ and ${}^{dv_{ds}}/_{dt}$ $\rightarrow \infty$ are assumed, i.e. $P_{sw,vi} = 0$ and

$$P_{sw} = P_{sw,oss} = f_{sw} V_{dc} Q_{oss}\big|_{V_{dc}} \overset{(1)}{=} f_{sw} \frac{V_{dc}^{1+|k|}}{a} \frac{1}{R_{ds,on}} \tag{2}$$

results. It can be noticed that $P_{cond} \propto R_{ds,on}$ while $P_{sw} \propto {}^{1}/_{R_{ds,on}}$, thus $P_{cond} \propto P_{sw}^{-1}$. In fact, for a fixed voltage, increasing the chip area to reduce $R_{ds,on}$ leads to a counter proportional increase of $C_{oss}$, consequently of $Q_{oss}$ and hence of $P_{sw}$ in the considered model.
The described trend is visible in **Fig. 3 (a)**, where $\eta$ of a Si phase-leg is illustrated as function of $f_{sw}$ and $R_{ds,on}$. Fixing $f_{sw}$, $P_{cond}$ and $P_{sw}$ vary as described, leading to a minimum $P_{semi}$, i.e. maximum $\eta$, when $P_{cond} = P_{sw}$. The weight breakdown analysis of modern power converters reveals that magnetic and filter components are the principal contributors to the overall weight. Since a higher $f_{sw}$ reduces the filtering effort (i.e. the size of magnetic and filter components), the maximum $f_{sw}$ ensuring the $\eta$-target is highlighted. $\eta = 99\,\%$ can only be reached if $f_{sw} < 28\,\text{kHz}$ even if the sole $P_{semi}$ is considered. The same calculations are repeated for a SiC phase-leg and the results are shown in **Fig. 3 (b)**. Since $\text{FoM}_{SiC}(1000\,\text{V}) = 92\,{}^{\text{MHz}}/_{\text{V}} \approx 10\,\text{FoM}_{Si}(1000\,\text{V})$, superior performance is expected. The $\eta$-target is shifted to $99.5\,\%$, assuming a more reasonable loss breakdown where $P_{semi}$ constitutes half of the overall allowed losses. Nevertheless, the $f_{sw}$-limit is increased by approximately a factor of 3 to 78 kHz. This preliminary result justifies the narrowing of the focus to wide bandgap semiconductors.

### *D. Multi-Cell Inverter Concepts*

The FoM based analysis of achievable $\eta$ and $f_{sw}$ confirms the superior performance of wide bandgap power semiconductors compared to Si, but does not take advantage yet of the benefit of the over-proportional voltage scaling of the FoM (cf. $|k| > 1$ in **Table II**). To evaluate this aspect, the performance of a generic multi-cell (e.g. Flying Capacitor or Modular Multi-Level) power converter concept is analyzed in this section adapting the previously developed procedure.
A phase-leg formed by the series connection of $N$ phase-leg cells, each rated for reduced power $P_{out,i} = {}^{P_{out}}/_{N}$ and DC voltage $V_{dc,i} = {}^{V_{dc}}/_{N}$, is considered to model the different multi-cell converter concepts. To deliver the same overall output power $P_{out,N} = P_{out} = N P_{out,i}$, $I_{out,i} = I_{out}$ is necessary. In the rest of the section, subscript $i$ defines a quantity relative to a single cell, whereas $N$ indicates the respective total for the complete phase-leg. Thus, $P_{semi,N}$

$$\begin{aligned} &= N(P_{sw,i} + P_{cond,i}) \\ &= N\left(f_{sw}\frac{({}^{V_{dc}}/_{N})^{1+|k|}}{a}\frac{1}{R_{ds,on}} + R_{ds,on}\left(\frac{2\sqrt{2}\,{}^{P_{out}}/_{N}}{{}^{V_{dc}}/_{N}}\right)^2\right) \\ &= \frac{P_{sw}}{N^{|k|}} + N P_{cond} \end{aligned} \tag{3}$$

is obtained and the optimum number of cells $N_{opt}$ can be derived as

$$\frac{\mathrm{d}P_{semi,N}}{\mathrm{d}N} = 0 \quad \xrightarrow{(3)} \quad N_{opt} = \sqrt[1+|k|]{\frac{|k| P_{sw}}{P_{cond}}}. \tag{4}$$

If $|k| = 1$ is assumed, $N_{opt} = \sqrt{{}^{P_{sw}}/_{P_{cond}}}$. The corresponding $P_{semi,N} = 2\sqrt{P_{sw} P_{cond}}$ features a minimum coinciding with $P_{semi}$. Consequently, if $|k| \leq 1$, multi-cell approaches would not be beneficial in terms of semiconductors performance.
In reality $|k| > 1$, hence, considering e.g. $N = 6$, $\text{FoM}_{GaN}({}^{1000\,\text{V}}/_{6} = 167\,\text{V}) = 1.26\,{}^{\text{GHz}}/_{\text{V}}$ is 2.3 times bigger than $6\,\text{FoM}_{SiC}(1000\,\text{V}) = 0.55\,{}^{\text{GHz}}/_{\text{V}}$, i.e. the FoM trends scale over-proportionally with respect to voltage. Accordingly, superior semiconductor performance is expected when multi-cell concepts are adopted.
Differently from Section II-C, in this case, for each ($f_{sw}$, $R_{ds,on}$)-pair, the corresponding $N_{opt}$ is derived according to (4) and considered in (3) to calculate $\eta$. $N_{opt}$ and $\eta$ are overlapped in **Fig. 3 (c)** to summarize the obtained results for a GaN phase-leg. GaN scales similarly to SiC according to the selected FoM, but GaN devices are available with lower $V_{ds,MAX}$, thus preferred in the multi-cell approach. It can be noticed that for high $f_{sw}$ and low $R_{ds,on}$ (i.e. high $Q_{oss}$) values, high $N_{opt}$ values are preferred to compensate for otherwise dominating $P_{sw}$, whereas the viceversa is true in the complementary half plane (low $f_{sw}$ and high $R_{ds,on}$ values).

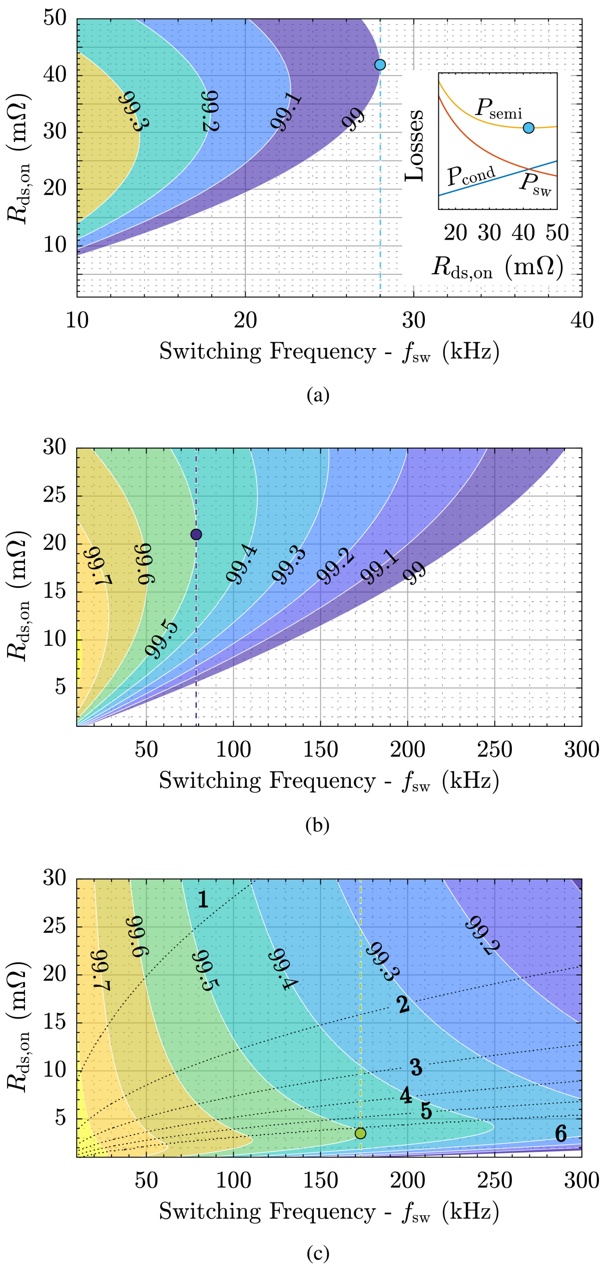


**Fig. 3:** The $\eta$-limit of (a) a Si, (b) a SiC and (c) a multi-cell GaN phase-leg ($V_{dc} = 1000\,\text{V}$ and $P_{out,phase} = 15\,\text{kW}$) as function of $f_{sw}$ and $R_{ds,on}$. $\eta = 99.5\,\%$ can only be achieved with wide bandgap semiconductors, i.e. (b) and (c), in the considered $f_{sw}$ range. The multi-cell approach enables a significant performance improvement compared to the conventional ones, maintaining the $\eta$-target up to $f_{sw} = 173\,\text{kHz}$ when $N = 6$.

$\eta = 99.5\,\%$ can be achieved with $f_{sw} = 173\,\text{kHz}$ and $N = 6$. $N$ is in fact limited to 6, since the modeled FoM unrealistically diverges to $\infty$ for higher values of $N$, leading to $\eta \rightarrow 100\,\%$. The selected ideal GaN semiconductor features $R_{ds,on} = 4\,\text{m}\Omega$ and $Q_{oss} \approx 210\,\text{nC}$.
Overall, significantly better semiconductors performance, e.g. $\eta > 99.5\,\%$ with $f_{sw} > 100\,\text{kHz}$, is achieved considering the multi-cell inverter concept. Volume and weight of the overall converter are assumed to reduce accordingly, since lower losses require lower cooling effort, i.e. smaller heat-sinks, and a higher $f_{sw}$ enables the downsizing of the filter and magnetic components.

## III. Reliability Analysis of Multi-Cell Inverters

Since decades, safe-failure and fault-tolerant mechanical systems relying on redundancy are the core of the aircraft design industry [24]. In parallel with the paradigm shift towards MEA, higher reliability, eventually exceeding the capability of conventional solutions, is nowadays also required in power converters for aerospace applications [25]. In fact, a reliable system in a critical environment, does not only guarantee the safety of its users, but as well reduces maintenance costs, extends operating times and avoids costly unexpected interruptions of service [26]. Nevertheless, efficiency and light-weight still maintain high priority among the specifications of power converters for aerospace applications [5], [6], arising the challenge of investigating topologies able to simultaneously combine all the mentioned features.

In this section, the reliability problem is formalized, defining the framework for the comparison of different multi-cell inverter topologies. Finally, it is proven how the optimization of multi-cell inverters cannot prescind from an accurate analysis of their reliability. The higher number of cells, in fact, significantly affects the reliability of the overall converter and this drawback can only be compensated by installing redundant elements, which negatively impact the power density.

### A. Reliability Model

A common approach to formalize reliability problems [27] is based on the definition of the reliability function of a component. $R_{\text{comp}}(t)$ states the probability that a component does not fail until time $t$, i.e. that it is able to perform its associated functions as intended and when required. The expectation of the continuous operating time of that component, i.e. the mean time between (to) failures (MTBF), is obtained from the area underlying $R_{\text{comp}}(t)$ as

$$\text{MTBF}_{\text{comp}} = \int_0^\infty R_{\text{comp}}(t)\text{d}t. \tag{5}$$

Assuming a constant failure rate $\lambda$ over time (only random failures occurring), a typical expression for $R_{\text{comp}}(t)$ is the unitary decaying exponential function

$$R_{\text{comp}}(t) = e^{-\lambda t}, \tag{6}$$

where $\lambda = 1/\text{MTBF}_{\text{comp}}$ since $\int_0^\infty e^{-\lambda t} = 1/\lambda$.

Engineering systems in critical environments are typically formed by the interconnection of several components and ensure high reliability by means of redundancy. In the interest of this analysis, systems formed by $K+Q$ components, where $K$ indicates the number of components necessary for the system to operate as intended and $Q$ is the number of installed redundant components, are considered. Moreover, all components are assumed to have the same $R_{\text{comp}}(t)$ (time dependency is omitted from now on). In this case, the reliability function of the system $R_{\text{sys}}$ can be calculated [26] as

$$R_{\text{sys}} = \sum_{r=K}^{K+Q} \binom{K+Q}{r} R_{\text{comp}}^{r}(1-R_{\text{comp}})^{K+Q-r}. \tag{7}$$

Finally, the mean time between failure of the system $\text{MTBF}_{\text{sys}}$ can be estimated applying the definition of MTBF (expressed in (5) for $R_{\text{comp}}$) to $R_{\text{sys}}$ obtained with (7). In case $K>1$ and $Q=0$ (system without redundancy), $R_{\text{sys}} = R_{\text{comp}}^K$ and $\text{MTBF}_{\text{sys}} = \text{MTBF}_{\text{comp}}/K$ can be significantly smaller than $\text{MTBF}_{\text{comp}}$. Differently, in case $K>1$ and $Q \geq 1$ (system with redundancy), $\text{MTBF}_{\text{sys}}$ can exceed $\text{MTBF}_{\text{comp}}$ depending on the ratio between $K$ and $Q$, i.e. the reliability of the system can exceed the one of the single component, as aimed for installing redundant elements.

### B. Redundancy in Multi-Cell Inverters

The developed reliability model is applied in this section to calculate the reliability functions characterizing two identified categories of multi-cell inverters. Conventional inverter solutions are not included in the comparison, since their performance is judged insufficient to meet the target defined by the aircraft industry.

From the system point-of-view, multi-cell three-phase inverters without redundant elements are modeled first as the series connection of $N$ identical components, i.e. phase-leg cells ($R_{\text{cell}}$, $\text{MTBF}_{\text{cell}}$), forming the phase-leg system ($R_{\text{p-l}}$). Hence, three identical phase-leg systems composed of $N$ cells each form the overall three-phase inverter system ($R_{\text{inv}}$, $\text{MTBF}_{\text{inv}}$). Thus, the total number of cells is $N_{\text{tot}} = 3N$, as shown in **Fig. 4 (a)** for $N=3$. The abstract concepts of component and system are therefore now transferred to the one phase-leg cell, to the three phase-legs and to the three-phase inverter.

*No Redundancy:* Since the functioning of a phase-leg in multi-cell inverters generally requires the correct operation of all $N$ cells forming it, $K=N$. Therefore, $R_{\text{p-l}} = R_{\text{cell}}^N$, $R_{\text{inv}} = R_{\text{p-l}}^3 = R_{\text{cell}}^{3N}$ and consequently $\text{MTBF}_{\text{inv}} = \text{MTBF}_{\text{cell}}/3N$. **Fig. 5** shows $R_{\text{cell}}$ (red) and $R_{\text{inv}}$ (black dashed) in case of $N=9$. $\text{MTBF}_{\text{inv}}$ can be compared to $\text{MTBF}_{\text{cell}}$ visualizing the reduction of area underlying the respective reliability functions.

*Phase-Leg Level Redundancy:* Inverter topologies such as Flying Capacitor (FCC) and Neutral Point Clamped (NPC) converters, which have a multi-cell but not a modular phase-leg structure, are grouped in this category. In this case, as shown in **Fig. 4 (b)**, redundancy can be introduced in a first approximation only by installing additional parallel phase-legs. Accordingly, $N_{\text{tot}}$ can be calculated as $N_{\text{tot,p-l}} = N(3+Q_{\text{p-l}})$. In case of failure, the faulty phase-leg can be disconnected and replaced by any (to simplify the derivation) redundant one. Even if more convenient strategies to handle certain types of failures are proposed in literature [28], for the purpose of this analysis only this generally valid approach is considered.

To update $R_{\text{inv}}$ in presence of redundancy, (7) must be computed with $R_{\text{comp}} = R_{\text{p-l}} = R_{\text{cell}}^N$, $K=3$ for the number of phases and any $Q = Q_{\text{p-l}} \geq 1$. The results for $Q_{\text{p-l}} = 1 \dots 3$ and $N=9$ are shown in yellow in **Fig. 5**. $Q_{\text{p-l}} = 3$ is indicated in yellow to highlight the corresponding $R_{\text{inv}}$. A weak increase of $\text{MTBF}_{\text{inv}}$ for each redundant phase-leg can be noticed.

*Cell-level Redundancy:* Inverter topologies such as Modular Multi-Level (MMLC) and Cascaded H-Bridge (CHB) converters are grouped in this category, since they feature a modular multi-cell phase-leg structure which allows to directly add redundant cells to each phase-leg, as shown in **Fig. 4 (c)**. Thus, $N_{\text{tot,c}} = 3(N+Q_{\text{c}})$. In case of failure, the faulty cell can be bypassed and a redundant one (installed in the same phase-leg) operated. Hence, $R_{\text{p-l}}$ can be calculated according to (7) with $R_{\text{comp}} = R_{\text{cell}}$, $K=N$ for the number of necessary cells and $Q = Q_{\text{c}} \geq 1$. $R_{\text{inv}}$ obtained as $R_{\text{p-l}}^3$ for $Q_{\text{c}} = 1 \dots 3$ and $N=9$ are shown in blue in **Fig. 5**, where $Q_{\text{c}} = 1$ is also indicated in blue to highlight the corresponding $R_{\text{inv}}$. A more significant increase of $\text{MTBF}_{\text{inv}}$ for each redundant cell can be noticed in this case.

### C. Effect of Redundancy on Power Density

The discussed modeling of the two considered redundancy approaches provides the basis to define the scaling trends in terms of power density of multi-cell inverters with respect to reliability.

To enable this evaluation, $\text{MTBF}_{\text{inv}}$ is calculated as described in the previous section for the cases featuring $Q_{\text{p-l}} = 0 \dots 3$, $Q_{\text{c}} = 0 \dots 3$ and $N = 3, 6$ and $9$. After computing the percentage ratio $\text{MTBF}_{\div} = 100\ \text{MTBF}_{\text{inv}}/\text{MTBF}_{\text{cell}}$, i.e. the ratio between the areas underlying each $R_{\text{inv}}$ and $R_{\text{cell}}$, the obtained results are shown in **Fig. 6** as function of $N_{\text{tot}}$. $\text{MTBF}_{\text{cell}}$ is technology and design dependent, therefore a relative expression for $\text{MTBF}_{\text{inv}}$, i.e. $\text{MTBF}_{\div}$, is preferred for the sake of generality. Since $\text{MTBF}_{\text{inv}} < \text{MTBF}_{\text{cell}}$ in all the cases, $\text{MTBF}_{\div} < 100\,\%$. The system diagrams help visualizing again the evolution of the circuits structure in presence of the two considered

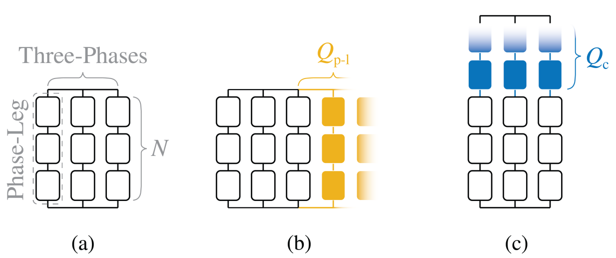


**Fig. 4:** System level structure of the considered multi-cell three-phase inverters in case $N=3$, comparing (a) no redundancy, (b) phase-leg level redundancy and (c) cell-level redundancy approaches.

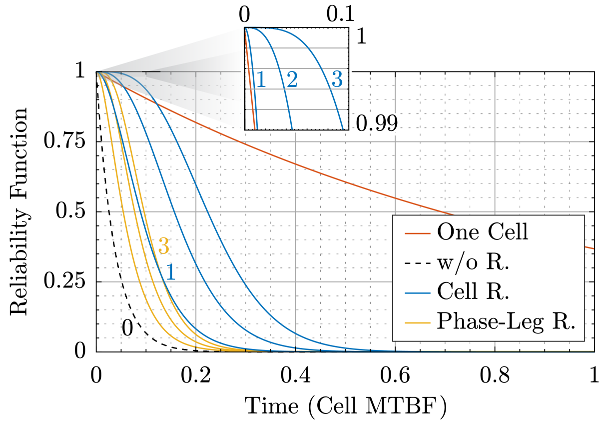


**Fig. 5:** $R_{\text{cell}}$ (red) and $R_{\text{inv}}$ either when no redundancy (black dashed), phase-leg level redundancy (yellow) or cell-level redundancy (blue) are considered. The area underlying the curves defines $\text{MTBF}_{\text{inv}}$ of the corresponding solution. The value of $Q$ associated to a certain $R_{\text{inv}}$ curve is indicated with matching colors.

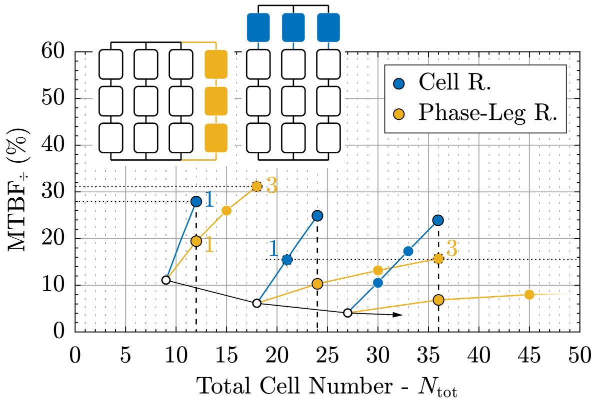


**Fig. 6:** $\text{MTBF}_{\div}$ for $Q_{\text{p-l}} = 1 \ldots 3$ (yellow), $Q_{\text{c}} = 1 \ldots 3$ (blue) and $N = 3$, 6 and 9 as function of $N_{\text{tot}}$. The white dots indicate $\text{MTBF}_{\div}$ with $Q = 0$. The system diagrams help visualizing the circuits structure in presence of the two levels of redundancy ($N = 3$, $Q_{\text{p-l}} = Q_{\text{c}} = 1$, $N_{\text{tot}} = 12$).

levels of redundancy: $N = 3$ and $Q_{\text{p-l}} = Q_{\text{c}} = 1$ ($N_{\text{tot}} = 12$) are shown as an example.

In the graph, white dots indicate $\text{MTBF}_{\div}$ with $Q = 0$, which follow the trend $N_{\text{tot}} = 3N$ and $\text{MTBF}_{\div} = {}^{100}/_{3N}\%$ highlighted by the arrow. Without redundancy, $\text{MTBF}_{\div}$ drops $\propto {}^{1}/_{N}$, e.g. resulting in $\text{MTBF}_{\text{inv}} \approx 4\,\%\ \text{MTBF}_{\text{cell}}$ already with $N = 9$ ($N_{\text{tot}} = 27$). Additionally, for a fixed value of $N$, two different splines (yellow and blue) describe the increasing trends of $\text{MTBF}_{\div}$, depending on $Q_{\text{p-l}}$ and $Q_{\text{c}}$ according to the proposed model. It can be noticed that the values of $\text{MTBF}_{\div}$ obtained with $Q_{\text{p-l}} = 3Q_{\text{c}}$ are comparable between each other, e.g. $\text{MTBF}_{\div} \approx 30\,\%$ for $N = 3$, $Q_{\text{p-l}} = 3$ and $Q_{\text{c}} = 1$. In fact, e.g. installing one redundant cell per phase-leg ($Q_{\text{c}} = 1$) or three redundant phase-legs ($Q_{\text{p-l}} = 3$) provides almost the same level of redundancy (cf. **Fig. 5**). Generally, increasing $Q$, the overall reliability is improved at the expense of increased $N_{\text{tot}}$.

For higher values of $N$, a second trend is identified in **Fig. 6**. Given the expressions of $N_{\text{tot,c}}$ and $N_{\text{tot,p-l}}$, it is clear that increasing $Q_{\text{c}}$ by 1 increases $N_{\text{tot,c}}$ by 3 (independently from $N$), whereas increasing $Q_{\text{p-l}}$ by the same amount increases $N_{\text{tot,p-l}}$ by $N$. This translates into significantly flatter slopes of the yellow splines for increasing $N$ or, in other words, to a much more severe impact of the phase-leg redundancy approach on the overall power density. A possible countermeasure to this drawback is identified in realizing each phase-leg as parallel connection of several phase-legs designed for reduced power. Although $N_{\text{tot}}$ would be significantly increased, the reduced power cells would have a smaller weight and/or volume and a better trade-off between power density and reliability might be found at the expense of increased complexity. Differently, for high values of $N$, the effect of increasing $Q_{\text{c}}$ (i.e. of cell-level redundancy) on the power density becomes even negligible.

Considering $Q_{\text{p-l}} = 3Q_{\text{c}}$ (e.g. $Q_{\text{c}} = 1$ and $Q_{\text{p-l}} = 3$), the two expressions describing the reduction of power density in converters adopting the two considered redundancy approaches are found as

$$\delta_{\text{p-l}} = \frac{3}{3 + Q_{\text{p-l}}}\delta_0 \quad \xrightarrow{Q_{\text{p-l}}=3} \quad \frac{\delta_0}{2} \tag{8}$$

and

$$\delta_{\text{c}} = \frac{N}{N + Q_{\text{c}}}\delta_0 \quad \xrightarrow{Q_{\text{c}}=1} \quad \frac{N}{N+1}\delta_0 \quad \xrightarrow{N>>1} \quad \delta_0, \tag{9}$$

for phase-leg and cell-level redundancies respectively. $\delta_0$ indicates the power density (with $Q = 0$) of a converter to which both redundancy approaches are ideally applicable. Consequently, $\delta_{\text{c}} \approx \delta_0 = 2\delta_{\text{p-l}}$ holds when $N >> 1$. Therefore, when targeting a high reliability figure in a power density optimized design, a converter topology where cell-level redundancy is possible must be generally preferred, since to guarantee the same level of redundancy, even twice the power density can be achieved (e.g. in case $Q_{\text{c}} = 1$ and $Q_{\text{p-l}} = 3$).

It is important to mention that a comparison in terms of power density and reliability of different converters should take into account as well the inevitably different designs of the cells forming them, since different designs might lead to incomparable power densities and reliability figures. However, this aspect is strictly related to the specifications and to the selected topologies, therefore cannot be discussed in general terms.

Moreover, although this analysis is limited to the power stage of the considered converters, it is worth mentioning that modularity is necessary and must be extended to the overall converter, e.g. to control and measurement circuits, not to introduce a different bottleneck in the increase of reliability [29].

### *D. MTBF versus Safe Operating Time*

The definition of MTBF introduced in Section III-A leads to $R_{\text{comp}}(\text{MTBF}_{\text{comp}}) = e^{-1} = 0.37$, i.e. when $t = \text{MTBF}_{\text{comp}}$ the component failure probability $1 - R_{\text{comp}} = 63\,\%$, unacceptable in the critical application of interest and independent of $\lambda$. A different reliability indicator, i.e. the Safe Operating Time (SOT), defined as the time at which $R_{\text{inv}}$ drops below a certain, still high (e.g. $99\,\%$), reliability threshold, can be introduced to better compare the different redundant multi-cell solutions with the single cell. The zoom of **Fig. 5**, highlighting $R_{\text{inv}} > 99\,\%$, shows how the cell-level redundancy approach (blue) with $N = 9$ and $Q_{\text{c}} \geq 1$ can even compete with the single cell (red) in terms of SOT, even if $\text{MTBF}_{\div} \approx 10\,\%$.

## IV. Modular Integrated Motor Drives

The two most common modular multi-cell inverter topologies, to which cell-level redundancy can be applied, are the CHB converter and the MMLC [26]. Unfortunately, severe limitations prevent their usage in power density oriented designs at the specified voltage and power ratings. The CHB converter requires an isolated, therefore inevitably bulky, DC voltage supply per cell while in the MMLC, a significant amount of capacitance needs to be installed at the DC side of each cell to compensate for the power pulsation. Control schemes regulating the flow of fluctuating circulating currents to limit this drawback enable a reduction of the capacitance requirements [30], however, they are still insufficient to meet the power density targets.

Additionally, it is worth mentioning that in applications involving electrical machines, the system reliability can also be compromised by a failure of the load, e.g. due to the damaging of the motor windings isolation, which is at least as likely to occur as the considered failures in the power stage [19]. For this reason, novel electric machine concepts often feature modular multi-phase stators with dedicated decoupled windings able to tolerate a confined failure [14]. Accordingly, a trend towards compact modular multi-cell inverters, providing a power electronics interface suitable to drive multi-phase electric machines, can be identified in literature labeled as Integrated Modular Motor Drives (IMMD) [15].

Advantageously, IMMD in combination with multi-phase machines not only improve the system reliability. IMMD, in fact, are typically embedded in the machine housing, e.g. on the end plate or on the surface of the stator iron, thus allowing to reduce the cables length, the electromagnetic emissions, design and installation costs and complexity, while increasing the system power density [31]. Since the mentioned benefits are the main design drivers in power electronics for the aerospace and automotive industries, lot of attention is nowadays placed on IMMD [32]. Minimizing the length of the cables connecting the inverter to the machine also prevents overvoltages due to waves reflection (which could occur in case of long cables), i.e. the limit on the maximum ${}^{\mathrm{d}v_{\mathrm{ds}}}/_{\mathrm{d}t}$ can be increased [19] reducing the occurring switching losses (cf. Section II-A). Adopting concentrated windings, a capacitive voltage divider rather than a transmission line best models the voltage distribution along the coil during a switching transient, i.e. the *first-turn* effect is not present [33]. Moreover, differently from the case of distributed windings, the maximum voltage difference between two adjacent turns is clearly defined and therefore the isolation requirements can be reduced [19]. Finally, if the amplitude of the switched voltage waveform of each cell is below the partial discharge inception voltage of conventional windings isolation (typically above $1\,\mathrm{kV}$, [33]), no drawback can be associated to high ${}^{\mathrm{d}v_{\mathrm{ds}}}/_{\mathrm{d}t}$, and output or ${}^{\mathrm{d}v}/_{\mathrm{d}t}$ filters can even be omitted pushing further the achievable power density.

A suitable IMMD converter topology combining all the mentioned advantages is the Stacked Polyphase Bridge (SPB) converter, originally developed for MV train applications twenty years ago [34], but recently re-proposed as an evolution of the Modular High-Frequency (MHF) converter [35]. As illustrated in **Fig. 7**, each cell is formed by a three-phase inverter, therefore no power pulsation occurs and the requirement of capacitance at the DC side of each cell can be significantly reduced. Since the cell element is commercially available both as power module or as integrated circuit (depending on the voltage and power ratings), the design effort is minimized and high availability is guaranteed. Moreover, with the integration of gate drivers in the power semiconductors packages [36], the power density of SPB converters can be pushed even further.

Several recent studies on the SPB converter proved the stability of its DC-link [37], developed modulation schemes improving the harmonic content of the input waveforms [38] and distributed control strategies [40] even able to bypass failures affecting one cell [39]. Given its modular and scalable phase-leg structure and power dense cell design, this topology is identified as the most favorable converter solutions to fulfill the targeted performance.

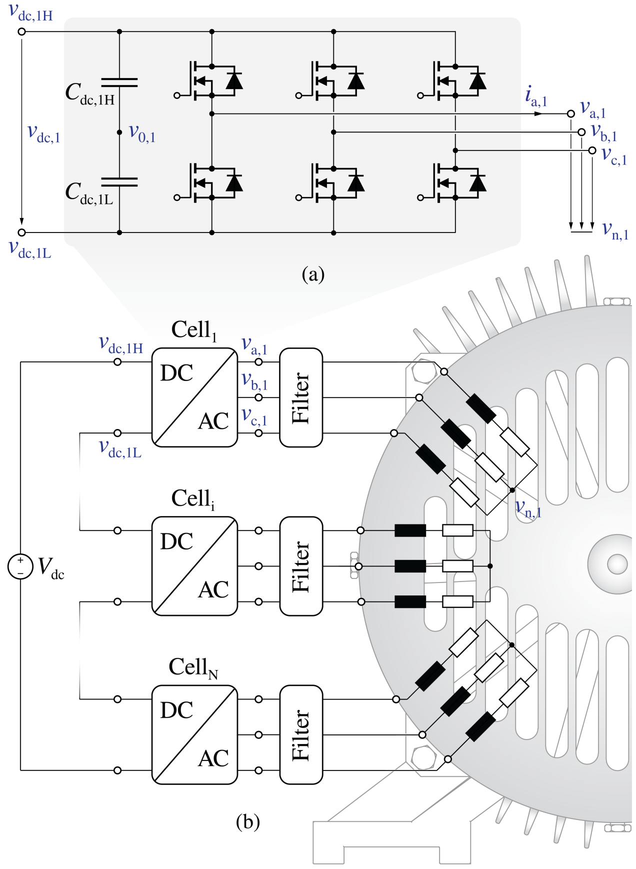


**Fig. 7:** Schematic of the SPB converter. The input series connection of (a) several identical three-phase inverter cells form the (b) modular multi-cell structure of the overall converter, e.g. suitable to drive multi-phase electric machines.

## V. Optimization of the SPB Inverter

In this section, the design of the SPB three-phase inverter is optimized with respect to gravimetric power density ($\gamma$) and efficiency ($\eta$) according to the specifications reported in **Table I**.

### A. Optimization Algorithm - Design Space

The design variables subject to optimization, the constraints defining their range of variation and the developed models computing the main contributions to the overall converter losses, weight and volume are summarized herein.

First, the number of series connected cells $N$ forming the SPB converter is varied from 1 to 7. A SPB converter with $N = 1$ is equivalent to a conventional three-phase inverter; this solution is considered only as benchmark for the multi-cell approaches. The nominal input voltage of each cell $V_{\mathrm{dc,i}} = {}^{V_{\mathrm{dc}}}/_{N}$, after considering a safety margin, defines the required power semiconductor voltage rating $V_{\mathrm{ds,MAX}}$. The best-in-class power device according to the considered FoM is selected for each value of $N$, as summarized in **Fig. 2** and **Table III**. Once the power stage is fixed, $f_{\mathrm{sw}}$ is varied from $50\,\mathrm{kHz}$ to $250\,\mathrm{kHz}$. In case an output $LC$ filter is desired, its corner frequency $f_{\mathrm{c}}$ is defined as the maximum frequency that guarantees enough attenuation to the $f_{\mathrm{sw}}$ harmonic component but still avoids that $f_{\mathrm{out}}$ related components can excite the resonance of the $LC$ filter elements (see **Table IV**). Several values of $L_{\mathrm{out,i}}$, logarithmically spaced in a range that avoids excessive inductor current ripple, capacitive current and inductive voltage drop are considered [44]. These constraints form the output filter design space highlighted in **Fig. 8** and defined in **Table IV**. The value of $C_{\mathrm{out,i}}$ is calculated according to $L_{\mathrm{out,i}}$ and $f_{\mathrm{c}}$. $C_{\mathrm{dc,i}}$ is defined solely to limit the voltage ripple on $V_{\mathrm{dc,i}}$ at $3f_{\mathrm{sw}}$. Additional constraints on $C_{\mathrm{dc,i}}$ defined by the application, e.g. energy storage requirements, are neglected, since do not affect the comparison in relative terms.

For each design derived from the combination of all the values assumed by the sweeping variables, all voltage and current waveforms in the converter are generated with accurate and computationally efficient analytical models. Hence, the losses in the power semiconductors are calculated according to the loss models described in Section II-A. Volume and weight of the power and gate driver PCBs are extrapolated from available hardware prototypes. Losses, weight and volume of auxiliary circuits, e.g. control and measurement, are estimated in the same way. The more significant losses, weight and volume of $L_{\mathrm{out}}$ are calculated and optimized by the software presented in [45]. Volume and weight of $C_{\mathrm{out,i}}$ and $C_{\mathrm{dc,i}}$ are derived from an exhaustive analysis of most commercially available electrolytic, film and multi-layer ceramic capacitors in the voltage range of interest. For the necessary capacitance value, the most compact available solution is selected. Volume and weight of the heat-sink are calculated with the CSPI method [46], considering $\mathrm{CSPI} = 15\,{}^{\mathrm{W}}/_{\mathrm{K\,dm^3}}$ and $\Delta T = 40\,^{\circ}\mathrm{C}$, values which are validated in [5].

### B. Optimization Results - Performance Space

The results of the described optimization procedure are summarized in the $\eta\gamma$-Pareto plot illustrated in **Fig. 9 (a)**. Only the approaches with $N = 1$, 2 and 6 are shown, since these designs correspond to the ones where the selected power devices are operated each at the maximum allowed voltage and therefore result in the best performing solutions. In this case, in fact, the advantage of over-proportional voltage scaling semiconductors performance can best compensate for the drawbacks associated to the increased value of $N$, e.g. in terms of weight. Both multi-cell designs ($N = 2$ and 6) outperform the conventional three-phase inverter ($N = 1$) as expected from the analysis derived in Section II-D. Although this more comprehensive study reasonably estimates more losses, the expected trends are validated. The selected design (highlighted in **Fig. 9 (a)** and described in **Table V**) features $\eta = 99\,\%$ and $\gamma = 22.8\,{}^{\mathrm{kW}}/_{\mathrm{kg}}$ (including output

**TABLE III:** Best-in-class power semiconductors.

| N | $V_{\mathrm{dc,i}}$ (V) | Power Semiconductor see **Fig. 2** | | $V_{\mathrm{ds,MAX}}$ (V) | $Q_{\mathrm{oss}}$ (nC) @ $V_{\mathrm{dc,i,MAX}}$ | $R_{\mathrm{ds,on}}$ (mΩ) @ 100 °C |
|---|---|---|---|---|---|---|
| $=1$ | 1 kV | *Wolfspeed* C2M0045170D | [41] | 1.7 kV | 284 | 68 |
| $\geq 2$ | 500 V | *Gan Systems* GS66516B-T | [42] | 650 V | 126 | 46 |
| $\geq 6$ | 167 V | *EPC* EPC2047 | [43] | 200 V | 82 | 10 |

**TABLE IV:** Parameters defining the $LC$ output filter design space.

| Parameter | Constraint | Value |
|---|---|---|
| $a_{\mathrm{f,out}}$ | $f_{\mathrm{c}} > a_{\mathrm{f,out}} f_{\mathrm{out}}$ | 4 |
| $a_{\mathrm{f,sw}}$ | $f_{\mathrm{c}} < {}^{f_{\mathrm{sw}}}/_{a_{\mathrm{f,sw}}}$ | 5 |
| $f_{\mathrm{sw,min}}$ | $a_{\mathrm{f,sw}} a_{\mathrm{f,out}} f_{\mathrm{out}}$ | 40 kHz |
| $a_{\mathrm{i,C}}$ | $I_{\mathrm{C,out}} < a_{\mathrm{i,C}} I_{\mathrm{out}}$ | 40 % |
| $a_{\mathrm{i,L}}$ | $I_{\mathrm{L,out,ripple}} < a_{\mathrm{v}} I_{\mathrm{out}}$ | 100 % |
| $a_{\mathrm{v}}$ | $V_{\mathrm{L,out}} < a_{\mathrm{v}} V_{\mathrm{out}}$ | 17 % |
| | $\sqrt{1/M^2_{\mathrm{index,MAX}} - \cos^2\phi_{\mathrm{MAX}}} + \sin\phi_{\mathrm{MAX}}$ | |

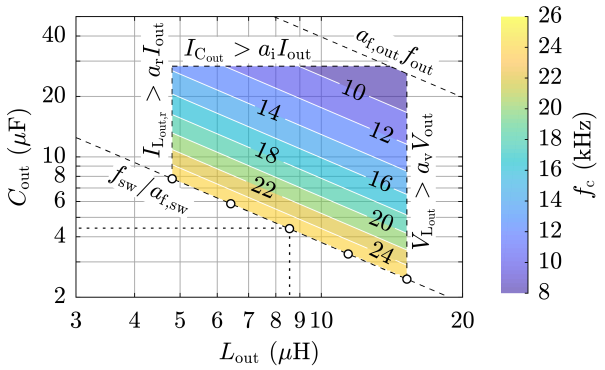

**Fig. 8:** $LC$ output filter design space defined by the constraints reported in **Table IV** relative to $f_{\mathrm{sw}}$ and $f_{\mathrm{out}}$, to the inductor current ripple, to the capacitive current and to the inductive voltage drop. White dots highlight the selected combinations of $L_{\mathrm{out}}$ and $C_{\mathrm{out}}$ for a given switching frequency.

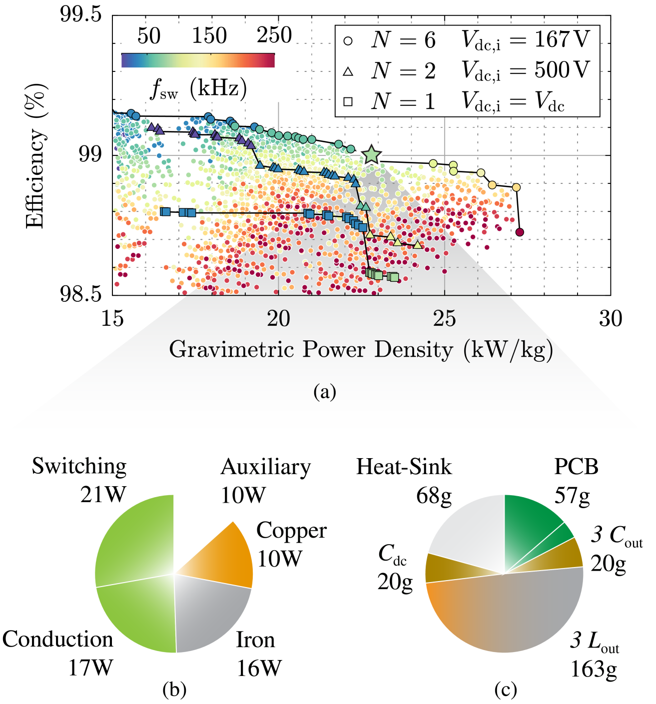


**Fig. 9:** (a) $\eta\gamma$-Pareto plot summarizing the results of the optimization of the three-phase SPB inverter. Both multi-cell solutions ($N=2$ and 6) outperform the conventional inverter ($N=1$). The selected design, featuring $\eta = 99\,\%$ and $\gamma = 22.8\,{}^{\mathrm{kW}}/_{\mathrm{kg}}$ (including output $LC$ filters) is highlighted. Details of the (b) loss and (c) weight breakdowns of a single cell are provided.

$LC$ filters), therefore meeting the aircraft industry targets (cf. **Fig. 1**). Details of its loss and weight breakdowns, relative to a single cell, are provided in **Fig. 9 (b)** and **(c)** respectively.

While the losses are almost evenly shared between the modeled sources, the weights are unequally distributed, with $L_{\mathrm{out}}$ responsible for $\approx 50\,\%$ of the cell weight. This prevents a further increase of $\gamma$ and is unexpected for a multi-cell converter. Typically, e.g. in FCC and MMLC, because of $V_{\mathrm{dc,i}} = {}^{V_{\mathrm{dc}}}/_{N}$ and of the equivalent $f_{\mathrm{sw}}$, i.e. $f_{\mathrm{sw,eq}} = N f_{\mathrm{sw}}$, the voltage-time area applied to $L_{\mathrm{out}}$ is reduced $\propto {}^{1}/_{N^2}$. Thus, the value of $L_{\mathrm{out}}$ can be reduced by $N^2$ still ensuring the same current ripple of an equivalent single-cell solution. Hence, if the volume of a magnetic component is assumed to be proportional to the energy stored in it, i.e. $vol[L] \propto {}^{1}/_{2} L I_{\mathrm{L}}^2$, also the volume (and approximately the weight) of $L_{\mathrm{out}}$ results reduced by $N^2$ and typically does not significantly contribute to the weight breakdown. In the case of the SPB converter, instead, the configuration of the cells do not enable the generation of $f_{\mathrm{sw,eq}}$ and the reduction by factor $N$ in the size of $L_{\mathrm{out}}$ enabled by $V_{\mathrm{dc,i}} = {}^{V_{\mathrm{dc}}}/_{N}$ is compensated by the necessity of $N L_{\mathrm{out}}$ elements per phase. Only the increase of $f_{\mathrm{sw}}$, consequence of the over-proportional voltage scaling of the FoM, allows to partially reduce the overall weight of the magnetic components. However, several motivations listed in Section IV lead to believe that the presence of output $LC$ filters is unnecessary in IMMD based on SPB converters. Thus, output $LC$ filter can be neglected and, as can be extrapolated from **Fig. 9 (c)**, double figures of $\gamma$ can be achieved.

Finally, it is worth commenting on the reliability performance of the designed modular multi-cell SPB converter. As discussed in Section III-D, given the reliability critical application of interest, the concept of SOT is preferred to the one of MTBF. As expected, the percentage ratio between the SOT of the multi-cell approach and the one of a single half-bridge cell, i.e. $\mathrm{SOT}_{\div}$, is very low when $Q_{\mathrm{c}} = 0$ ($\approx {}^{100}/_{3N}\%$, similarly to $\mathrm{MTBF}_{\div}$) and it worsens with increasing $N$ (i.e. $5.56\,\%$ with $N = 6$). However, with $Q_{\mathrm{c}} = 1$ and considering $\mathrm{SOT}_{\div}$ at the time at which $R_{\mathrm{inv}} = 99.73\,\%$ ($\pm 3\sigma$ confidence range), the selected SPB design results even 2.5 times more reliable than a single half-bridge cell. In this case, $\gamma$ is only partially affected, i.e. reduced to $19.5\,{}^{\mathrm{kW}}/_{\mathrm{kg}}$ (9). The calculated $\mathrm{SOT}_{\div}$ for all the values of $N$ considered in **Fig. 9 (a)**, different values of $Q_{\mathrm{c}}$ and confidence intervals are reported in **Table VI** together with the associated values of the $\gamma$-limit ensuring $\eta = 99\,\%$. As a consequence of the selected modular multi-cell topology, high $\mathrm{SOT}_{\div}$ values can be reached even with high values of $N$ at reduced cost in terms of $\gamma$ and $\eta$.

## VI. Conclusion

Meeting next generation aerospace requirements in terms of efficiency, gravimetric power density and reliability of power converters demands a breakthrough in power electronics designs, since a significant improvement is necessary compared to the state-of-the-art. The identified over-proportional voltage scaling characterizing the power semiconductors performance suggests to investigate multi-cell approaches, which as well typically enable the downsizing of the magnetic components. Unfortunately, the increased circuit complexity dramatically lowers the power converters reliability figures and the

**TABLE V:** Parameters of the selected Pareto design.

| **Parameter** | **Description** | **Value** | **Note** |
|---|---|---|---|
| $N$ | number of cells | 6 | |
| $V_{\mathrm{dc,i}}$ | cell input voltage | 167 V | |
| $f_{\mathrm{sw}}$ | switching frequency | 110 kHz | |
| $L_{\mathrm{out}}$ | output inductor | 5 µH | E25/10 Kool M$\mu$® |
| $C_{\mathrm{out}}$ | output capacitor | 10 µF | 200 V MMLC |
| $C_{\mathrm{dc}}$ | input capacitor | 30 µF | 200 V MMLC |

**TABLE VI:** SOT$_{\div}$ and $\gamma\big|_{\eta=99\,\%}$ as function of $N$ and $Q_{\mathrm{c}}$.

| | | **SOT$_{\div}$ (%) with $N$-$Q_{\mathrm{c}}$ cells** | | | | | |
|---|---|---|---|---|---|---|---|
| **$R_{\mathrm{inv}}$(SOT)** | | **1-0** | **2-0** | **2-1** | **6-0** | **6-1** | **6-2** |
| 0.9545 | $\pm 2\sigma$ | 33.3 | 16.7 | 164 | 5.56 | 62.8 | 159 |
| 0.9973 | $\pm 3\sigma$ | „ | „ | 650 | „ | 246 | 978 |
| 0.9999 | $\pm 4\sigma$ | „ | „ | 3340 | „ | 1260 | 8540 |
| $\gamma\big\|_{\eta=99\,\%}$ | | – | 19.3 | 12.9 | 22.8 | 19.5 | 17.1 |

introduction of redundant elements to compensate for this issue negatively affects the power density.

In this paper, different multi-cell topologies are evaluated, considering as reference the specifications of a 45 kW three-phase inverter for aerospace applications. Among them, modular solutions, able to achieve reliability figures comparable with the ones of conventional inverters, but still maintaining significantly higher performance, are preferred. The Stacked-Polyphase-Bridge (SPB) converter is selected among the others, since it provides multiple three-phase outputs and therefore can be combined with multi-phase machines as an Integrated Modular Motor Drive (IMMD), also reducing system design complexity and installation costs. A SPB three-phase inverter is finally optimized: a 6 cells design, featuring GaN power semiconductors, independent $LC$ filters and heat-sinks, can achieve an efficiency of 99 % at a gravimetric power density of $22.8\,{}^{\mathrm{kW}}/_{\mathrm{kg}}$ ($19.2\,{}^{\mathrm{kW}}/_{\mathrm{kg}}$ adding one redundant cell) when switching at 110 kHz. The set performance target is reached and high reliability is ensured, justifying the interest and highlighting the potential of the presented topology.

## References


[1] X. Roboam, B. Sareni, and A. D. Andrade, "More Electricity in the Air," *IEEE Ind. Electron. Mag.*, vol. 6, no. 4, pp. 6–17, 2012.

[2] "*Airbus*, *Rolls-Royce*, and *Siemens* to Develop Flying Demonstrator," siemens.com/innovation/en/home/pictures-of-the-future/mobility-and-motors/the-future-of-mobility-e-fan-x.html, accessed: 2018-07-01.

[3] "*Airbus*, *Rolls-Royce*, and *Siemens* Develops Hybrid-Electric Demonstrator," leehamnews.com/2017/11/29/airbus-rolls-royce-siemens-develops-hybrid-electric-demonstrator/, accessed: 2018-07-01.

[4] P. Korbinian, "Electric Propulsion Components with High Power Densities for Aviation," Presentation at Transformative Vertical Flight Workshop, Santa Clara County, CA, USA, 2015.

[5] *Research and Innovation Action, I2MPECT*, European Commission - Innovation and Networks Executive Agency, 4 2015.

[6] "*NASA* Government Contract NNX14AL79A," government-contracts.insidegov.com/l/9684390/NNX14AL79A, accessed: 2018-01-24.

[7] R. C. N. Pilawa-Podgurski, "Hybrid Switched Capacitor Power Converters Increasing Power Density Through New Circuit Topologies and Control Methods," Presentation at ETH Zurich, Zurich, Switzerland, 2017.

[8] C. Gammeter, F. Krismer, and J. W. Kolar, "Weight and Efficiency Analysis of Switched Circuit Topologies for Modular Power Electronics in MEA," in *Proc. of the IEEE 42nd Annual Conference on the Industrial Electronics Society (IECON 2016)*, Florence, Italy, 2016.

[9] A. Lesnicar and R. Marquardt, "An Innovative Modular Multilevel Converter Topology Suitable for a Wide Power Range," in *Proc. of the IEEE Power Tech Conference*, Bologna, Italy, 2003.

[10] J. Bourdon, P. Asfaux, and A. M. Etayo, "Review of Power Electronics Opportunities to Integrate in the More Electrical Aircraft," in *Proc. of the International Conference on Electrical Systems for Aircraft, Railway, Ship Propulsion and Road Vehicles (ESARS 2015)*, Aachen, Germany, 2015.

[11] T. Modeer, C. B. Barth, N. Pallo, W. H. Chung, T. Foulkes, and R. C. Pilawa-Podgurski, "Design of a GaN-based, 9-level Flying Capacitor Multilevel Inverter with Low Inductance Layout," in *Proc. of the IEEE Applied Power Electronics Conference and Exposition (APEC 2018)*, San Antonio, TX, USA, 2018.

[12] K. Sharifabadi, L. Harnefors, H.-P. Nee, S. Norrga, and R. Teodorescu, *Design, Control, and Application of Modular Multilevel Converters for HVDC Transmission Systems*. John Wiley and Sons, Ltd., 2016.

[13] O. Alavi, A. Hooshmand Viki, and S. Shamlou, "A Comparative Reliability Study of Three Fundamental Multilevel Inverters Using Two Different Approaches," *Electronics*, vol. 18, no. 5, 2016.

[14] E. Levi, "Multiphase Electric Machines for Variable-Speed Applications," *IEEE Trans. Ind. Electron.*, vol. 55, no. 5, pp. 1893–1909, 2008.

[15] T. M. Jahns and H. Dai, "The Past, Present, and Future of Power Electronics Integration Technology in Motor Drives," *CPSS Transactions on Power Electronics and Applications*, vol. 2, no. 3, pp. 197–216, 2017.

[16] D. Bortis, D. Neumayr, and J. W. Kolar, "$\eta\rho$-Pareto Optimization and Comparative Evaluation of Inverter Concepts Considered for the GOOGLE Little Box Challenge," in *Proc. of the IEEE 17th Workshop on Control and Modeling for Power Electronics (COMPEL 2016)*, Sapporo, Japan, 2017.

[17] Y. Lobsiger, "Closed-Loop IGBT Gate Drive and Current Balancing Concepts," Ph.D. dissertation, ETH Zurich, Zurich, Switzerland, 2014.

[18] D. Neumayr, M. Guacci, D. Bortis, and J. W. Kolar, "New Calorimetric Power Transistor Soft-Switching Loss Measurement Based on Accurate Temperature Rise Monitoring," in *Proc. of the IEEE 29th International Symposium on Power Semiconductor Devices and ICs (ISPSD 2017)*, Sapporo, Japan, 2017.

[19] *Motor Insulation Voltage Stresses under PWM Inverter Operation*, GAMBICA/BEAMA Technical Guide, 3 2016.

[20] M. Guacci, D. Bortis, I. F. Kovačević-Badstübner, U. Grossner, and J. W. Kolar, "Analysis and Design of a 1200V All-SiC Planar Interconnection Power Module for Next Generation More Electrical Aircraft Power Electronic Building Blocks," *CPSS Transactions on Power Electronics and Applications*, vol. 2, no. 4, pp. 320–330, 2017.

[21] M. Kasper, D. Bortis, and J. W. Kolar, "Scaling and Balancing of Multi-Cell Converters," in *Proc. of the IEEE International Power Electronics Conference (IPEC ECCE Asia 2014)*, Hiroshima, Japan, 2014.

[22] J. W. Kolar, J. Biela, and J. Minibock, "Exploring the Pareto Front of Multi-Objective Single-Phase PFC Rectifier Design Optimization - 99.2 % Efficiency vs. 7kW/dm$^3$ Power Density," in *Proc. of the IEEE 6th International Power Electronics and Motion Control Conference (IPEMCC 2009)*, Wuhan, China, 2009.

[23] J. Azurza Anderson, L. Schrittwieser, C. Gammeter, G. Deboy, and J. W. Kolar, "Relating the Figure of Merit of Power MOSFETs to the Maximally Achievable Efficiency of Converters," *to be published*, 2018.

[24] L. Manfriani, "Aircraft Systems," Presentation at ETH Zurich, Zurich, Switzerland, 2017.

[25] S. Rubino, R. Bojoi, A. Cavagnino, and S. Vaschetto, "Asymmetrical Twelve Phase Induction Starter Generator for More Electric Engine in Aircraft," in *Proc. of the IEEE Energy Conversion Congress and Exposition (ECCE USA 2016)*, Milwaukee, WI, USA, 2016.

[26] S. Busse, M. Hiller, K. Kahlen, and P. Himmelmann, "MTBF Comparison of Cutting Edge Medium Voltage Drive Topologies for Oil and Gas Applications," in *Proc. of the Petroleum and Chemical Industry Conference Europe (PCIC Europe 2015)*, London, UK, 2015.

[27] J. E. Huber and J. W. Kolar, "Optimum Number of Cascaded Cells for High-Power Medium-Voltage AC-DC Converters," *IEEE Journal of Emerging and Selected Topics in Power Electron.*, vol. 5, no. 1, 2017.

[28] J. Amini and M. Moallem, "A Fault-Diagnosis and Fault-Tolerant Control Scheme for Flying Capacitor Multilevel Inverters," *IEEE Trans. Ind. Electron.*, vol. 64, no. 3, pp. 1818–1826, 2016.

[29] D. Jiang, P. Ning, R. Lai, Z. Fang, and F. Wang, "Modular Design Method for Motor Drives," *Chinese Journal of Electrical Engineering*, vol. 4, no. 1, 2018.

[30] X. She, A. Huang, X. Ni, and R. Burgos, "AC Circulating Currents Suppression in Modular Multilevel Converter," in *Proc. of the IEEE 38th Annual Conference on Industrial Electronics Society (IECON 2012)*, Montreal, QC, Canada, 2012.

[31] P. Brockerhoff, Y. Burkhardt, K. Egger, and H. Rauh, "Highly Integrated Drivetrain Solution: Integration of Motor, Inverter and Gearing," in *Proc. of the 4th International Electric Drives Production Conference (EDPC 2014)*, Nuremberg, Germany, 2014.

[32] P. Brockerhoff, W. Schön, P. Blaha, P. Václavek, and Y. Burkhardt, "Disc Inverter in Highly Integrated 9-Phase Drivetrain for E-mobility," in *Proc. of the IEEE 17th European Conference on Power Electronics and Applications (EPE ECCE Europe 2015)*, Geneva, Switzerland, 2015.

[33] M. Denk and M. M. Bakran, "Partial Discharge Measurement in a Motor Winding fed by a SiC Inverter How Critical is High $\mathrm{d}v/\mathrm{d}t$ Really?" in *Proc. of the International Exhibition and Conference for Power Electronics, Intelligent Motion, Renewable Energy and Energy Management (PCIM Europe 2018)*, Nuremberg, Germany, 2018.

[34] R. Deplazes, "Neue transformatorlose Schaltungstopologie für Traktionsantriebe auf der Basis von 3-Stern-Asynchronmaschinen," Ph.D. dissertation, ETH Zurich, Zurich, Switzerland, 1999, (in German).

[35] L. Lambertz, R. Marquardt, and A. Mayer, "Modular Converter Systems for Vehicle Applications," in *Proc. of the E-Mobility - Electrical Power Train Conference*, Leipzig, Germany, 2010.

[36] "*Navitas* Products," navitassemi.com/products, accessed: 2018-07-01.

[37] M. Nikouie, O. Wallmark, L. Jin, L. Harnefors, and H.-P. Nee, "DC-Link Stability Analysis and Controller Design for the Stacked Polyphase Bridges Converter," *IEEE Trans. Power Electron.*, vol. 32, no. 2, pp. 1666–1674, 2017.

[38] L. Jin, S. Norrga, O. Wallmark, and M. N. Harnefors, "Control and Modulation of the Stacked Polyphase Bridges Inverter," in *Proc. of the IEEE Energy Conversion Congress and Exposition (ECCE USA 2014)*, Pittsburgh, PA, USA, 2014.

[39] L. Jin, S. Norrga, O. Wallmark, and N. Apostolopoulos, "Communication-Based Distributed Control of the Stacked Polyphase Bridges Converter," *IEEE Trans. Ind. Electron.*, vol. 65, no. 2, pp. 1011–1020, 2017.

[40] Z. Pan, M. Schweizer, G. Shrestha, and V.-M. Leppnen, "Cell Voltage Balancing of a Series-Connected Multiphase BLDC Motor Drive," in *Proc. of the IEEE 43rd Annual Conference of the IEEE Industrial Electronics Society (IECON 2017)*, Beijing, China, 2017.

[41] *C2M0045170D*, *Cree*, 06 2016.

[42] *GS66516B*, *Gan Systems*, 2018, Rev. 180422.

[43] *EPC2047*, *EPC*, 03 2017.

[44] M. M. Antivachis, D. Bortis, and J. W. Kolar, "Optimal DC-Link Referenced Output Filter Design for Three-Phase Inverters," *to be published*, 2018.

[45] P. Papamanolis, F. Krismer, and J. W. Kolar, "Minimum Loss Operation of High-Frequency Inductors," in *Proc. of the IEEE Applied Power Electronics Conference and Exposition (APEC 2018)*, San Antonio, TX, USA, 2018.

[46] J. W. Kolar, U. Drofenik, J. Biela, M. L. Heldwein, H. Ertl, T. Friedli, and S. D. Round, "PWM Converter Power Density Barriers," in *Proc. of the IEEE Power Conversion Conference (PCC 2007)*, Nagoya, Japan, 2007.